

STUDY OF CREEP OF ALUMINA-FORMING AUSTENITIC STAINLESS  
STEEL FOR HIGH-TEMPERATURE ENERGY APPLICATIONS

A Thesis

Submitted to the Faculty

in partial fulfillment of the requirements for the

degree of

Master of Science by

Natalie Petrovna Afonina

Thayer School of Engineering

Dartmouth College

Hanover, New Hampshire

September 2016

Examining Committee:

Chairman \_\_\_\_\_

(Dr. Ian Baker)

Member \_\_\_\_\_

(Dr. Rachel Obbard)

Member \_\_\_\_\_

(Dr. Harold Frost)

---

F. Jon Kull

Dean of Graduate Studies

Thayer School of Engineering

Dartmouth College

“Study of creep of alumina-forming austenitic stainless  
steel for high-temperature energy applications”

Natalie Petrovna Afonina

Master of Science

Dr. Ian Baker

Dr. Rachel Obbard

Dr. Harold Frost

## **ABSTRACT**

## **LIST OF TABLES**

Table 1: Abc .....15

Table 2: Abc .....32

## **LIST OF FIGURES**

Figure 1: Abc .....	15
Figure 2: Abc.....	27

## CHAPTER 1 INTRODUCTION

### 1.1 Background

Increasing efficiency while decreasing the cost of operating advanced power plants has been an ongoing process. Energy efficiency gains in fossil energy conversion and combustion system applications also result in the added benefit of reducing CO<sub>2</sub> emissions, bolstering the motivation to pursue efficiency-increasing strategies <sup>1-4</sup>. The efficiency of energy conversion applications is a strong function of steam temperature and pressure, thus increases in energy efficiency can be realized by elevating operating steam temperatures and pressures <sup>5</sup>. An increase in operating temperatures from 600 °C to 800 °C results in an efficiency increase of more than 10%. Efforts are currently underway to enable advanced power plants to function at temperatures greater than 700 °C. An important contributor to realizing these higher steam temperatures and pressures is the material composition of the power plants' industrial gas turbine components, super heater tubes and boilers <sup>6</sup>. Currently, many energy production and chemical processing plants operate at temperatures below 600 °C due to the poor performance of martensitic and ferritic steel alloys at higher temperatures <sup>7</sup>. To withstand the high temperature and pressure demands of energy applications, metal alloys must have the necessary material properties to withstand such conditions. These properties include the materials' high-temperature long term creep strength, oxidation and corrosion resistance and strength. Aggressive environments, where metal components are exposed to water vapor, sulfur and carbon species, are a prime target for new materials being developed <sup>8</sup>.

Nickel-based superalloys and austenitic alloys with high nickel concentrations perform well and have the necessary creep strength and oxidation and corrosion

resistance to withstand such conditions, but are prohibitively expensive and not economically viable except for use in specialized applications due to the high levels of nickel and nickel cost<sup>3,4</sup>. Thus other alloys are now being researched and developed that can withstand the demands of such energy conversion and combustion systems as well as to decrease reliance on costly nickel-based alloys. However, in order for an alternative to be viable, it must have the strength, long-term creep and oxidation resistance close to or exceeding this of nickel-based alloys. One promising class of alloys that are low in cost and potentially capable of withstanding the rigors placed on the materials by high temperature energy applications are alumina-forming austenitic stainless steels (AFAs)<sup>6,9-15</sup>. However, it has not yet been demonstrated that this class of steels have the oxidation and corrosion resistance as well as creep strength necessary to be a viable alternative to nickel-based alloys.

## 1.2 Alumina-Forming Austenitic Stainless Steels

Extensive efforts are underway to improve the high-temperature strength, corrosion and oxidation resistance, and long-term creep resistance of AFAs, ideally at lower cost compared with currently used materials. Researchers at Oak Ridge National Laboratory have developed a new family of AFAs in the last few years that have yielded promising results for use with elevated temperatures above 700 °C in aggressive environments<sup>8,10,14,16,17</sup>. These new AFAs being developed have a composition range of Fe-(12-35)Ni-(12-15)Cr-(2.5-4)Al-(0.6-3)Nb (wt %), and include alloying additions such as Al, Cr, Mn and Ni to maintain a single phase austenitic matrix microstructure<sup>14</sup>.

The alumina ( $\text{Al}_2\text{O}_3$ ) layer that forms in AFAs at temperatures between 600 °C and 900 °C, acts as a protective barrier and increases the oxidation and corrosion

resistance of the material. Austenitic steels without sufficient additions of aluminum use chromia ( $\text{Cr}_2\text{O}_3$ ) scales as a protective layer, but in environments with high concentrations of water vapor and other oxidizing agents, the chromia scales perform poorly. Relatively small amounts of aluminum additions to austenitic steels have the ability to form the protective alumina surface layer. It's been shown that these alumina scale formations remain stable at operating temperatures between 650 °C and 800 °C, with the necessary oxidation resistance in environments with water vapor present, making AFAs the preferred choice for use in low-cost, high-temperature structural materials<sup>6,9,18–22</sup>. Ferritic FeCrAl alloys have excellent oxidation and corrosion resistance at elevated temperatures, however at temperatures greater than 600 °C their creep resistance does not meet expectations set by nickel-based alloys, a property that is attributed to their open body-centered-cubic (b.c.c) structure<sup>14</sup>.

Precipitates play a large role in determining the mechanical properties of an alloy. Both the type of precipitate and their distribution have an effect on an alloy's strength and creep resistance. Precipitate nucleation occurs due to the strain energy being lowered<sup>23</sup>. Precipitates nucleate preferentially on grain boundaries due to a larger strain energy reduction compared with precipitation occurring on dislocations, which has a higher activation energy<sup>24</sup>. The type, size, distribution and volume fraction all have an effect on the alloy's properties. The effect of various precipitates and their phases on creep strength in AFAs with a variety of alloying elements is still being explored to identify the optimum combination of alloys and precipitates for their use at elevated temperatures in the 600 °C to 800 °C range. Small changes in alloy composition and precipitate phases often result in a wide variation of creep strengths<sup>5,15,25</sup>.

### 1.3 AFA precipitates

In the past, AFAs have primarily used MC carbides (with the metal primarily being niobium) or  $\gamma'$ -Ni<sub>3</sub>Al for their strength<sup>8,10</sup>. Particles that are  $\sim$ 10 nm in size are effective at increasing creep strength by pinning dislocations in the f.c.c. austenitic matrix. However at elevated temperatures above 800 °C, the carbide precipitates coarsen and dissolve<sup>26</sup>, making them unsuitable for strengthening purposes in elevated temperature applications. Newer grades of AFAs being developed have an austenitic face-centered-cubic matrix instead of a b.c.c matrix, and their elevated temperature creep resistance and strength is achieved through not only the existing MC carbides and  $\gamma'$ -Ni<sub>3</sub>Al precipitates, but also Fe<sub>2</sub>Nb Laves phase and NiAl-type B2 precipitates<sup>6,14,27-29</sup>.

Intermetallic phase precipitates have the potential to be used as strengtheners in AFA alloys to further improve their creep resistance. The formation of Fe<sub>2</sub>Nb Laves phase precipitates along grain boundaries in ferritic steels results in a decrease in the alloys' strength<sup>30</sup>. In contrast, creep strengthening has been achieved in AFAs<sup>8,31</sup>. For example the AFA alloy Fe-20Cr-30Ni-2Nb-5Al (at%) demonstrates good ductility and strength, even with extensive intermetallic formation of C14 Laves phase precipitates along the grain boundaries<sup>32</sup>. It has been shown that in Fe-20Cr-(25–35)Ni-2Nb (at.%) alloys, fine dispersions of strengthening Fe<sub>2</sub>Nb Laves phase can form within the austenitic iron matrix<sup>33</sup>. The use of Fe<sub>2</sub>Nb Laves phase particles has shown thermal stability up to its melting point of 1640 °C in the Fe-Nb system over a prolonged duration<sup>34</sup> and exists in equilibrium with f.c.c.  $\gamma$ -Fe above 955 °C in the Fe-Cr-Ni base steel<sup>35</sup>, making it a good candidate for strengthening AFAs at elevated temperatures.

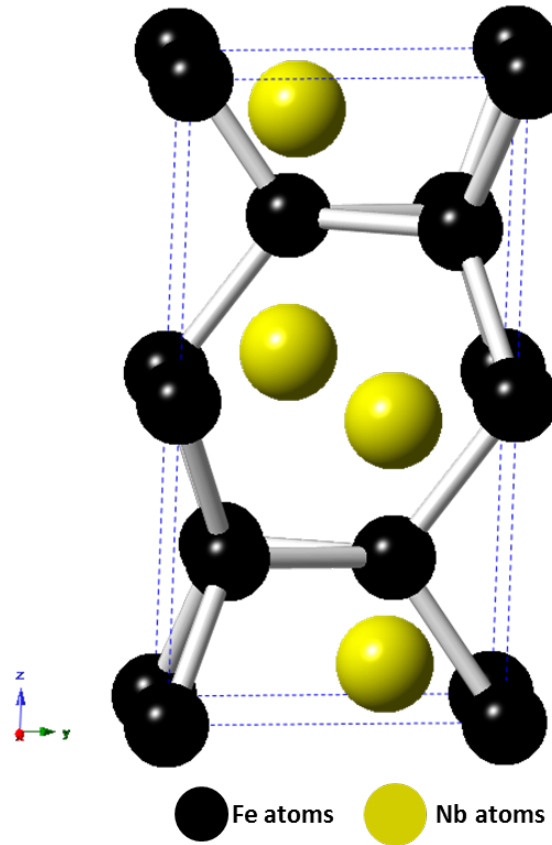


Figure 1.1: Diagram of the C14 Fe<sub>2</sub>Nb (AB<sub>2</sub>) Laves phase structure. Niobium represents the A atoms and iron the B atoms.

Prior work with the intermetallic Laves phase Fe<sub>2</sub>Nb has shown that the strengthening effect of the precipitate is dependent on if it precipitates on grain boundaries or in the austenitic matrix, and in what volume fractions and particle size it appears in the alloy <sup>16</sup>. See figure 1.1 for a diagram depicting the hexagonal C14 Fe<sub>2</sub>Nb (AB<sub>2</sub>) Laves phase structure. As the Laves phase particles increase in density and size, the brittle property of the precipitate causes the material to lose its strength and creep resistance. Thus, a fine particle dispersion diameter of <100 nm is recommended to match the creep strength exhibited by AFAs strengthened with MC carbides and prevent failure of the material <sup>16</sup>. This decrease in the precipitate size and increase of the

precipitate volume fraction in the austenitic matrix, allows for dislocations to be pinned leading to an increase in the alloy's creep strength. It has recently been shown that in Fe-20Cr-30Ni-2Nb (at.%), the alloy's long-term creep resistance increased with an increasing area fraction of Laves phase precipitated on the grain boundary. It was also noted that dislocations that piled up near Laves phase grain boundaries were effective at suppressing local deformation by inhibiting the motion of dislocations and thereby increasing the long-term creep strength of the alloy <sup>36,37</sup>. This creep-strengthening mechanism was coined "*grain boundary precipitation strengthening mechanism*" by Tarigan et al.

Yamamoto et al found that in addition to Fe<sub>2</sub>Nb Laves phase forming, after heat treating at 750 °C, dense and fine B2-type NiAl (AB) precipitates formed in the  $\gamma$ -Fe matrix and on the grain boundaries <sup>17</sup>. The B2-type NiAl phase particles were dark in contrast and between 300 nm to 1  $\mu$ m in size. The Fe<sub>2</sub>Nb-type Laves phase particles appeared spherical with a bright contrast in the matrix and less than 500 nm in size. See Figure 1.2 for an example of precipitate contrast in Fe-20Cr-30Ni-2Nb-5Al (at. %). At elevated temperatures, B2-type NiAl precipitates play an important role in providing corrosion and oxidation resistance by acting as an aluminum reservoir for formation of the alumina protective layer <sup>38</sup>. They are not effective in improving the high-temperature tensile strength at temperatures greater than 400 °C <sup>39,40</sup>, however it's been posited that B2-type NiAl precipitates improve creep resistance by affecting the climb of dislocations in the matrix or the precipitate's resistance to dislocation slicing <sup>17</sup>.

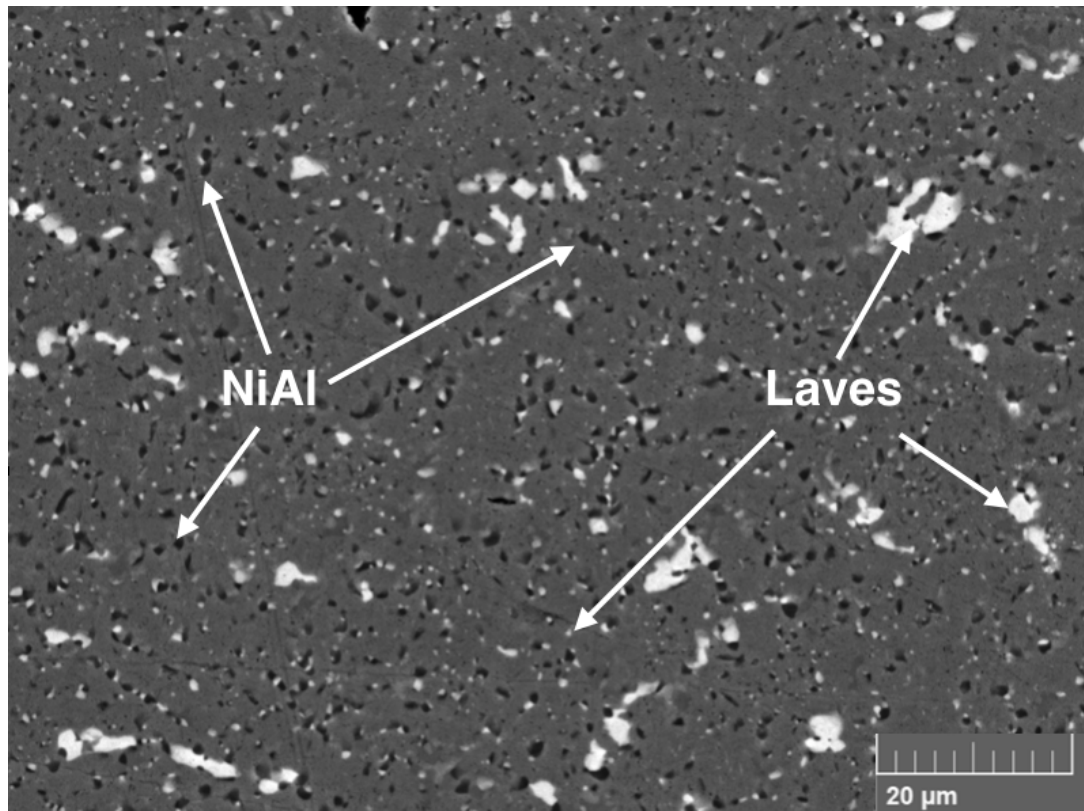


Figure 1.2: Backscattered electron images showing  $\text{Fe}_2\text{Nb}$  Laves phase (light contrast) and B2-type NiAl phase (dark contrast) precipitates in the matrix of Fe-20Cr-30Ni-2Nb-5Al (at. %) homogenized at 1250 °C and heat-treated at 800 °C for 240 h.

In order to better predict which precipitates are most beneficial for increasing AFA high temperature creep strength, further tests and characterizations need to be performed to form a better understanding of the complex interactions between the presence of various precipitates and phases and their effect on the alloys' creep properties.

## 1.5 Outline of Research Project

The purpose of this thesis is to investigate the high-temperature strengthening mechanisms in alumina-forming austenitic stainless steels, specifically the high

temperature constant-stress creep and mechanical properties of the model alloy Fe-20Cr-30Ni-2Nb-5Al (at. %) at different aging conditions.

The investigation proceeded as follows:

- 1) A constant-stress creep apparatus was designed, built and validated
- 2) Samples were prepared from the model alloy and aged for time intervals of 0, 2.4, 24 or 240 h at 800 °C
- 3) Constant-stress creep tests were conducted at elevated temperatures of 760 °C
- 4) Secondary electron imaging was used to examine the microstructure of the samples prior to, during and after the completion of creep testing
- 5) Elevated temperature tensile tests were conducted on aged samples at 760 °C

Chapter 2 covers materials preparation, the design, construction, validation and testing procedure of a constant-stress creep apparatus, and materials characterization techniques.

Chapter 3 details the effect of aging time on the microstructural evolution and high temperature constant-stress creep behavior of the model alloy. The observed microstructural changes and precipitate evolution prior to, during and after creep tests were conducted, are analyzed and discussed.

Chapter 4 details the effect of aging time on the high temperature tensile behavior of the alloy. The observed differences of the mechanical properties of the alloy at different aging conditions is analyzed and discussed.

In Chapter 5 and 6, the conclusions of this research project are summarized and suggestions are made for future work.

## CHAPTER 2 EXPERIMENTAL METHODS

### 2.1 Introduction

This chapter details materials preparation and processing methods, the design and testing of a constant-stress creep apparatus, and materials characterization techniques involved in this work.

### 2.2 Materials Preparation

#### 2.2.1 Materials Used

The alloy Fe-20Cr-30Ni-2Nb-5Al (at.%) was used for both the creep and strain-rate jump tests throughout this study. The alloy was provided by Carpenter Technology Corporation (Wyomissing, PA). A split-cast vacuum induction melting heat was used to cast the alloy into tapered ingots. The ingots were then press forged into rectangular bars with the following dimensions: 0.625" x 0.75" x 24". The chemical composition of the alloy was analyzed by LECO combustion analysis and X-ray Fluorescence. Table 2.1 compares the analyzed element compositions with the theoretically calculated weight percent ratios, demonstrating agreement between the predicted and actual chemical composition of the cast alloy.

*Table 2.1 Chemical composition comparison of the Carpenter Technology alloy*

<b>Element Analyzed</b>	<b>Theoretical (wt%)</b>	<b>Analyzed (wt%)</b>
Nickel	31.88	31.9
Chromium	18.83	18.98
Niobium	3.36	3.34
Aluminum	2.44	2.48
Carbon	0.00	0.02
Cobalt	0.00	0.01
Copper	0.00	<0.01
Manganese	0.00	<0.01
Molybdenum	0.00	0.01
Phosphorus	0.00	<0.005
Silicon	0.00	<0.01
Sulfur	0.00	<0.001

### *2.2.2 Sample Machining*

In preparation for both creep testing and strain-rate jump tests, the alloyed material was machine milled and then sectioned with a saw. The TRAK DPM SX3P bed mill with a 40 taper spindle and ProtoTRAK SMX control was used with zinc-coated carbide end mills to mill the specimens into the T-bone shapes necessary to insert into the specimen grips of the creep testing and strain-rate jump testing machines as shown in Figure 2.1. To ensure the accurate geometry of each T-bone, the specimen was sectioned using coolant with a Model 650 Low Speed Diamond Wheel Saw from South Bay Technology, Inc.

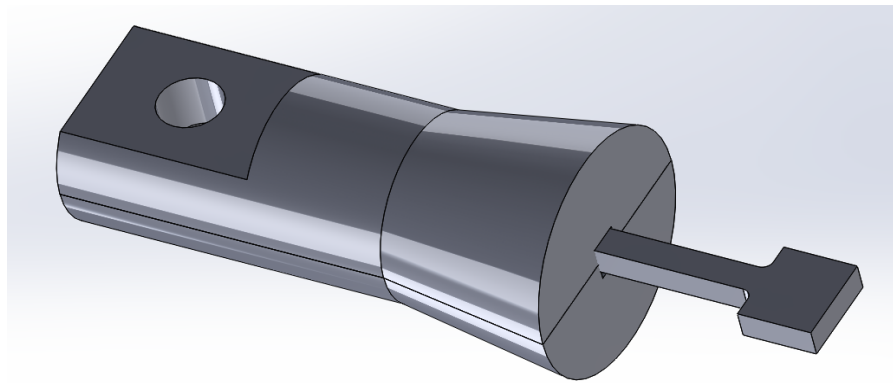


*Figure 2.1: CAD file drawing of a T-bone specimen inserted into one side of the creep machine's specimen grips.*

### *2.2.3 Material Homogenization and Heat Treatments*

Solutionizing anneals were necessary to homogenize the material for a uniform microstructure. For all tests in this study, the as-cast model alloy was homogenized for 24 h at 1250 °C in a vacuum and then water-quenched. This temperature and time was chosen with consideration to prior work with Fe-20Cr-30Ni-2Nb-5Al, where it was determined that a solutionized single phase  $\gamma$ -matrix could be consistently formed. This was confirmed with SEM images of the as-cast raw material and compared with the material after a heat treatment homogenization conducted at 1250 °C for 24 h.

All solutionizing heat treatments were conducted using a Thermo Scientific Type 54233 Lindberg Closed-Shell tube furnace. Specimens were placed on top of a piece of alumina and maneuvered to the center of the furnace tube with a rod. The furnace tube was then purged with argon and placed under a pressure of 0.01 MPa to maintain an oxygen-free environment and to prevent oxidation of the sample inside the furnace until the heat treatment was complete. Once the sample was sealed inside the furnace, the furnace was turned on and the temperature set to 1250 °C. When the

solutionizing anneal was complete, the pressure seal was broken and the sample rapidly quenched in water with a substantially greater mass compared to the sample.

All heat treatments of the samples after they were homogenized were conducted at 800 °C for a variety of time intervals of 0, 2.4, 24 or 240 h. Heat treatments were conducted in a Barnstead Thermolyne Type 47900 Furnace. Samples were placed inside an alumina crucible and then positioned at the center of the furnace for the duration of the heat treatment. At the completion of the heat treatment, the samples were quenched with water.

## 2.3 Constant-Stress Creep Apparatus Design and Testing

### 2.3.1 *Overview of constant-stress creep testing*

Creep testing machines take several forms depending on what is the primary target of investigation, which includes constant load, variable stress and constant-stress rigs. A small change in the level of stress can have a large effect on strain rate affecting both the overall creep rate and microstructure of the sample. With increasing strain, the cross-sectional area  $A$  of a test specimen decreases, which if tested in a constant-load creep rig, results in an increase in the instantaneous stress. With a load  $P$ , cross-sectional area  $A$ , the stress on the specimen will be  $\sigma = P/A$ . A constant-stress machine would allow the stress variable to be controlled by compensating for the decrease in the specimen's cross-sectional area by decreasing the effective load applied on the specimen. This allows the basic creep mechanisms acting on the specimens tested to be isolated and analyzed.

The curve of the constant-stress cam is key to constructing a precise, operational constant-stress creep apparatus. In Figure 2.2, a schematic layout of the

weight-transferring system is shown for a constant-stress creep test applications. For constant-load creep tests, the curved cam would be circular.

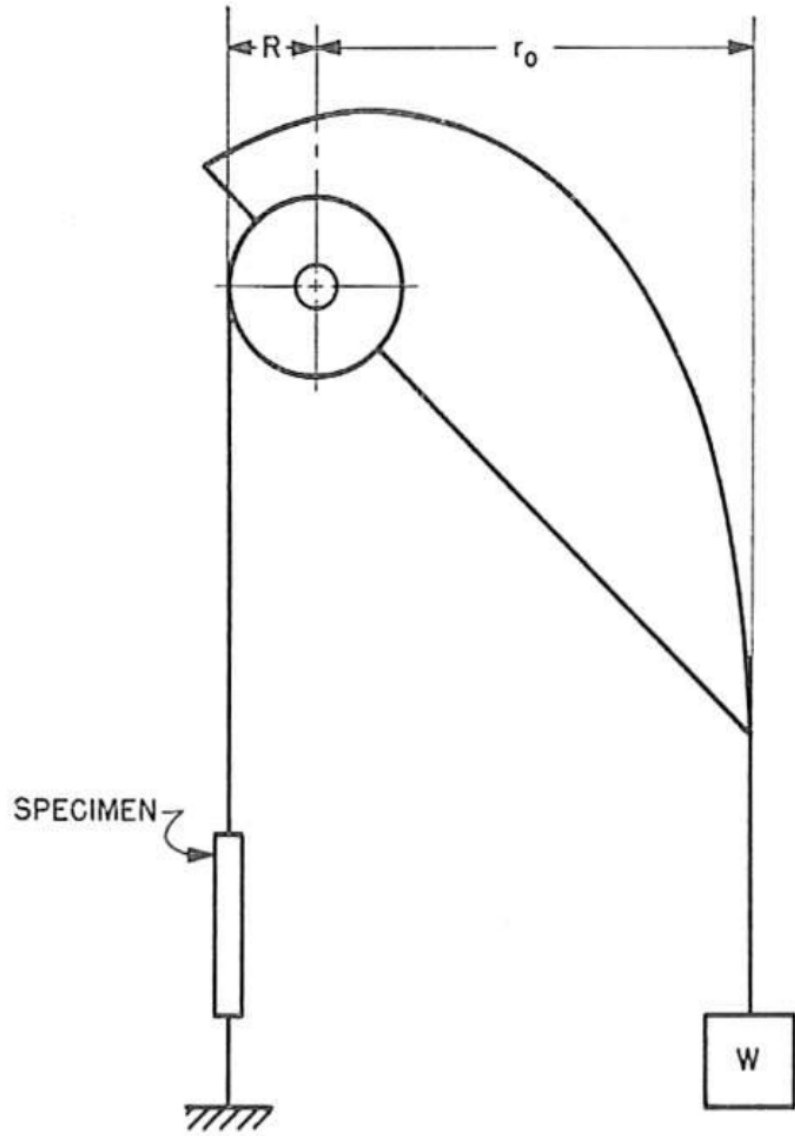


Figure 2.2: A schematic diagram detailing a weight-transferring system used for constant-stress creep tests.<sup>41</sup>

The curved profile of the constant-stress cam is analytically calculated using a system of parametric equations following the outline of an Andrade-Chalmers beam<sup>42</sup>. It is shown that the fixed Cartesian coordinates  $x$  and  $y$  of a constant-stress cam can be

written in terms of constants and the angle  $\theta$  (see Appendix I for derivation of equations (1) and (2)), where  $\theta$  is the angle the cam makes with the horizontal as seen in Figure 2.3 from the paper by Garofalo et al (1962). In equations (1) and (2)  $L_0$  is the initial specimen gauge length prior to creep,  $r_0$  is the initial moment arm,  $R$  is the radius of the smaller load-transferring wheel. The Cartesian coordinates from which the profile of the cam can be traced for machining are determined by the values of constants  $a$  and  $b$ :

$$x = \frac{a}{1 + b\theta} \left[ \cos(\theta) + \frac{b \sin(\theta)}{1 + b\theta} \right] \quad (1)$$

$$y = \frac{a}{1 + b\theta} \left[ \sin(\theta) - \frac{b \cos(\theta)}{1 + b\theta} \right] \quad (2)$$

$$\text{Where: } a = \frac{r_0 L_0}{L_0 - R\theta_0} \quad \text{and} \quad b = \frac{R}{L_0 - R\theta_0}$$

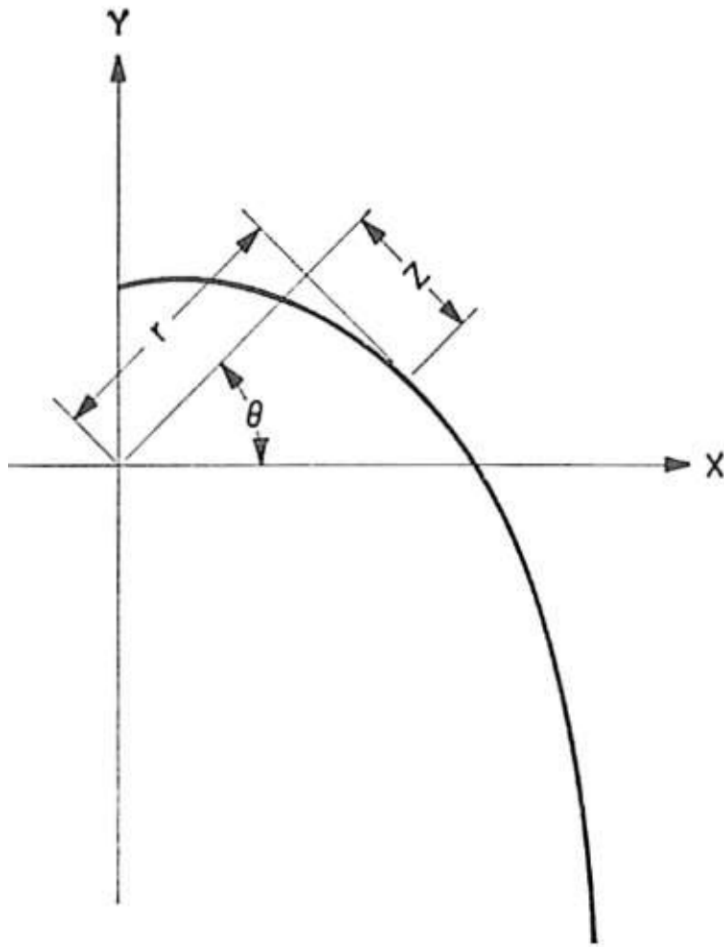


Figure 2.3: A diagram detailing the coordinate system used for the cam profile

For the purposes of this investigation, a constant-stress creep test rig was custom-designed, built and validated based on the methods developed by Garofalo, Richmond and Domis (1962). The following section discusses the system's dimensions, assembly, cam parameters, calibration and testing procedure.

### 2.3.2 Design of Creep Test rig

As discussed in the previous section, the cam profile is dictated by the constants  $a$  and  $b$ . For a small load-transferring wheel with a radius of 0.75 inches, an initial specimen gauge length of 0.787 inches and a desired mechanical advantage of 8:1,

the values of  $a = 6.00$  in and  $b = 0.95$  in. Using the derived equations (1) and (2) and the calculated values of  $a$  and  $b$ , the Cartesian coordinates of the cam's profile in  $x$  and  $y$  can be calculated for a given angle  $\theta$  as shown in Table 2.2.

*Table 2.2 Coordinates for the constant-stress cam profile fabricated for use in this study, with  $a = 6.00$  in and  $b = 0.95$  in.*

$\Theta$ (deg)	x (in)	y (in)
-20	4.06	-15.13
-15	5.10	-11.87
-10	5.66	-9.35
-5	5.93	-7.34
0	6.00	-5.72
5	5.94	-4.37
10	5.80	-3.24
15	5.59	-2.29
20	5.33	-1.48
25	5.05	-0.79
30	4.74	-0.20
35	4.42	0.30
40	4.09	0.74
45	3.75	1.10
50	3.41	1.41
55	3.08	1.67
60	2.74	1.89
65	2.42	2.06
70	2.10	2.19
75	1.78	2.29
80	1.48	2.35
85	1.19	2.39
90	0.92	2.40
95	0.65	2.39
100	0.40	2.36
105	0.17	2.31
110	-0.05	2.24
115	-0.26	2.15
120	-0.45	2.05
125	-0.62	1.94
130	-0.78	1.82
135	-0.92	1.69
140	-1.05	1.55
145	-1.16	1.41
150	-1.25	1.26
155	-1.33	1.11

A photograph of the full assembly of the creep rig is shown in Figure 2.4 with a sample specimen in tension and placed under a 35 MPa load.

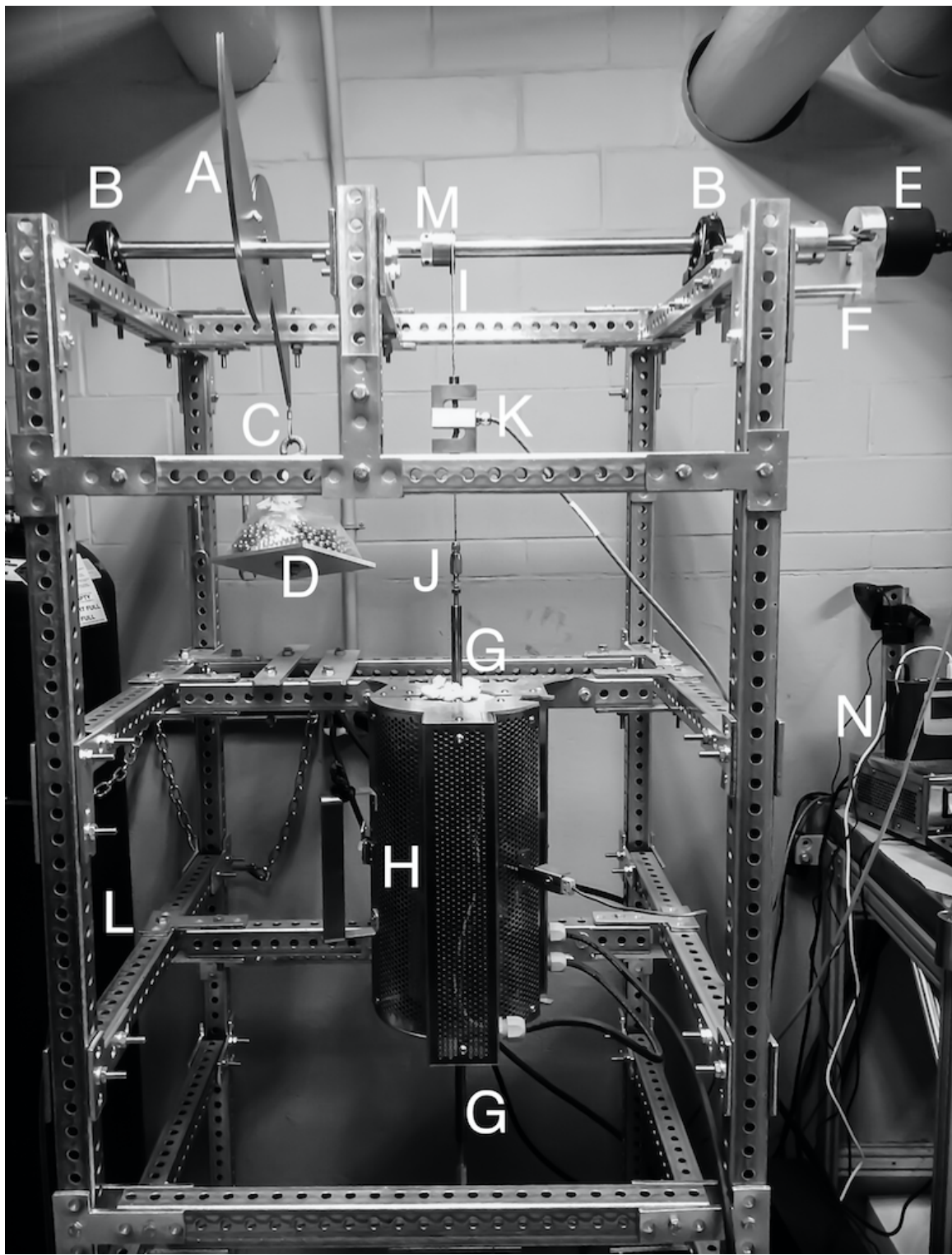


*Figure 2.4: Photograph of the constant-stress creep machine with system components labeled matching the key*

### Key for Figure 2.4

- A. Constant-stress cam
- B. Bearing pillow block
- C. Cable attached to load
- D. Load weight on loading tray
- E. Angular Displacement Transducer (ADT)
- F. ADT support
- G. Connecting rod
- H. Mellen Furnace
- I. Cable attached to specimen
- J. Swageless Thread Terminal
- K. Linear variable differential transformer (LVDT)
- L. Steel Frame
- M. Load-transferring wheel
- N. Data Logger

*\* Letters in parentheses () indicate machine components as per Figure 2.4*

The metal frame (L) of the rig is made of 1.5-in galvanized steel perforated tubing for heavy duty telescoping framing and is bolted onto four base mounts to account for uneven floor surfaces. The metal frame additionally supports the Mellen Inc. SCR Split Series 120 V 1200 W Furnace (H) mounted vertically. The furnace utilizes clamshell-heating elements capable of 1250 °C in air. The temperature is measured with a centrally located K-type thermocouple and controlled by a Mellen Inc. PS105 programmable power control cabinet. Two heavy-duty ball bearing pillow blocks (B) are

rigidly attached to the steel frame and support a 0.75-in diameter steel rod that acts as the cam and load-transferring wheel support shaft.

The constant-stress cam (A) and the load-transferring wheel (M) are mounted on the steel rod with a diametrical interference fit of 0.003-in, which facilitates free circular movement around the rod. The cam profile shown in Figure 2.2 is duplicated, inverted and attached to the original cam profile to balance the cam assembly when it's threaded onto the support rod. The small radius load-transferring wheel is designed for an 8:1 mechanical advantage. Both the cam and the wheel are attached to the center support shaft with a collet and two set screws placed on opposing sides and screwed in to firmly secure the components and eliminate movement when the system is under load. The cam and the load-transferring wheel are fabricated from 1018 steel. Appendix II contains CAD drawings with specifications of the cam and load-transferring wheel.

The TransTek Inc. Series 600 Model 0603-0000 Angular Displacement Transducer (ADT) with 100 mV/ $^{\circ}$  output and maximum usable range of  $\pm 40^{\circ}$  is attached (E) with a set screw to the end of the support shaft extending 1 inch past the pillow block and steel frame tubing. The ADT allows for measuring specimen elongation by tracking the angular displacement of the cam shaft as the sample lengthens throughout the duration of a creep test. More specifically, as the specimen creeps, the relative displacement of the two specimen grips is detected by the ADT. This angular displacement is translated into an electrical signal, which is then amplified by the TransTek Inc. Series D100 Dual DC 12VDC Power Supply and sent by the readout wire to the Grant Instruments Ltd. SQ2010 Portable Universal Input Squirrel Data Logger (N) to monitor, measure and record the elongation of the specimen. The

high accuracy ADT is capable of measuring an angular displacement of  $\pm 0.10\%$ , which translates to measuring a linear displacement of  $<0.001$  in. The ADT is supported with an aluminum bolted frame (F) to eliminate any torque placed on the high-precision measurement equipment.

Both the constant-stress cam and the load-transferring wheel have a 0.047-in radius milled groove on their outlines to create a track that allows for a 3/32-in wire cable to fit and wrap around with a snug fit. A wire 3/32-in cable (C) is attached to the constant-stress cam through a pinhole, shown in Figure 2.5, and swaged together with wire rope sleeves. The other end of the cable is swaged in the form of a loop and permits the attachment of a dead-weight load. The load is attached through the use of an 8-inch long metal hook threaded through the center of an aluminum 6x6-in square platform (D). The load is stacked on the platform. The material used for the applied load consists of steel 1/4-in diameter balls to aid in applying a variety of loads with precision.

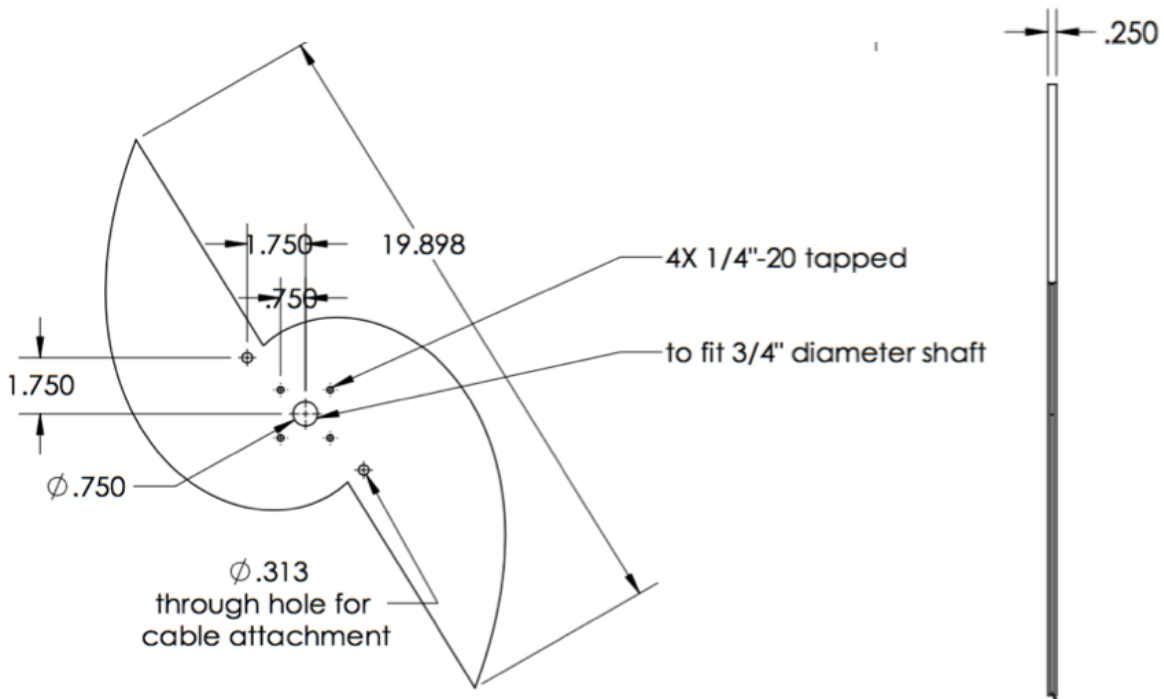


Figure 2.5: Design drawing of constant-stress cam

One end of a wire 3/32-in cable (I) is attached and swaged through a pinhole to the load-transferring wheel (M) on the opposite side that the cable is attached to the constant-stress cam. The other end of the cable drops vertically down to connect through two attachment openings in the vertically aligned Omega Engineering Inc. LC101-500: 500 lb S-beam load cell (K), which acts as the linear variable differential transformer (LVDT). The LVDT output wires are connected to the data logger (N) and Omega Engineering Inc. DP25B-S-A series Digital Panel Meter with a 4-digit LED display that aids in adjusting the cam placement when a load is applied by displaying the output in lbf units. A wire cable is attached through the bottom of the LVDT to a swageless thread terminal (J).

The thread terminal is screwed into the machined upper extension connecting rod (G). The extension rod is screwed into the upper male end of the machined specimen grips as shown in Figure 2.6. The specimen grips and connecting rods are fabricated from 718 Inconel to prevent elongation when heated in the furnace, and hold the specimen in a vertically aligned position. The lower specimen grips are similarly connected to an extension rod, a swageless thread terminal and a wire cable. Figure 2.6 shows a diagram of the details of the specimen grips. Appendix II contains CAD design drawings of the grip components, which includes the inner grips, collets, yolks, and rod connectors.

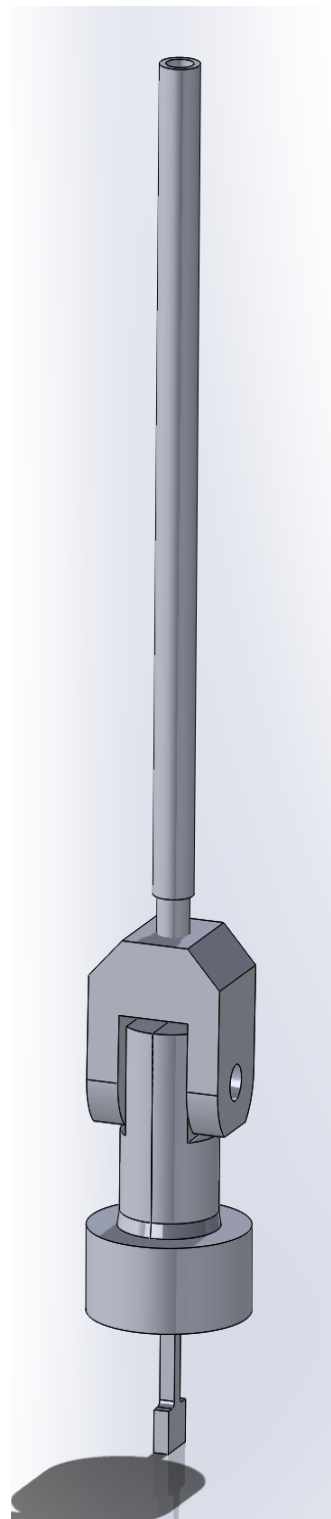
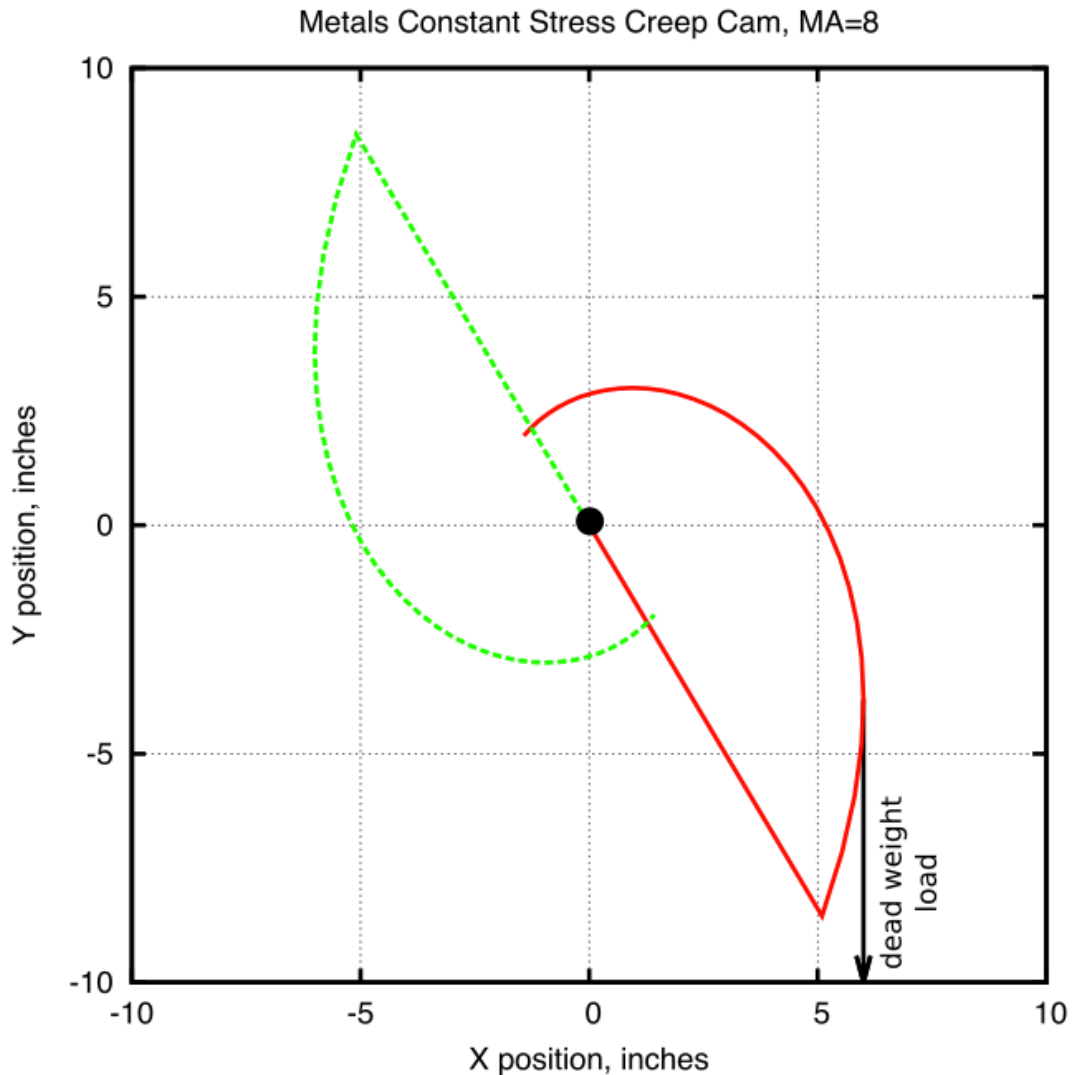


Figure 2.6: Diagram of specimen grips

Completing the linkage, the wire cable is vertically secured to the bottom crossbeam of the steel frame in a 1/4-in diameter slot to allow for lateral movement and adjustments of up to 2 inches when a load is applied to the system and the cable is placed under tension.

Of special note is the horizontal position mark that is inscribed on the constant-stress cam prior to the system assembly. The cam is designed to produce a constant-stress about this centerline as shown in Figure 2.7, which aids in proper adjusting and positioning of the cam during calibration testing such that the rig functions as intended (refer to Calibration of rig section 2.3.3).



*Figure 2.7: Plot of the constant-stress cam geometry. The cam's centerline is centered on  $y = 0$ .*

The Squirrel data logger receives amplified voltage readouts from the ADT and LVDT. The output is sampled at five-second intervals and then logged as an average of five samples. This logging rate allows for long term creep tests to be conducted by decreasing the amount of data logger memory used, while ensuring the data collected has appropriate resolution for detailed data analysis.

### 2.3.3 Calibration and Testing of rig

Breadths of tests were performed on the creep rig to determine that the system functioned as intended. The machine was calibrated for use with a load of 35 MPa, and a series of tests were conducted to prove that the load on the test sample would be reduced at the specified rate to produce a constant-stress.

The Angular Displacement Transducer (ADT) output is a voltage, which is converted to an angular displacement in degrees. This rotational displacement value is used to calculate the elongation of the test specimen to a high degree of precision. The ADT displacement measurements required an adjustment factor to match the actual test specimen elongation. To conduct the test and acquire the adjustment factor, a sample test specimen was placed in the system and the effective load was decreased in 5 lbf increments by mechanically simulating a displacement of the specimen, which was accomplished by unscrewing the upper connecting rod out of the upper specimen grip connector. The data logger was used to record the angular displacement recorded by the ADT, and a micrometer was used to measure and record the simulated linear displacement. The test was conducted three times and the data was averaged. Figure 2.8 shows the results of this calibration. When the ADT results were adjusted with a factor of 3.156, the displacement values were identical to those taken with the micrometer, demonstrating that the displacement measuring system accurately measured and recorded specimen elongation.

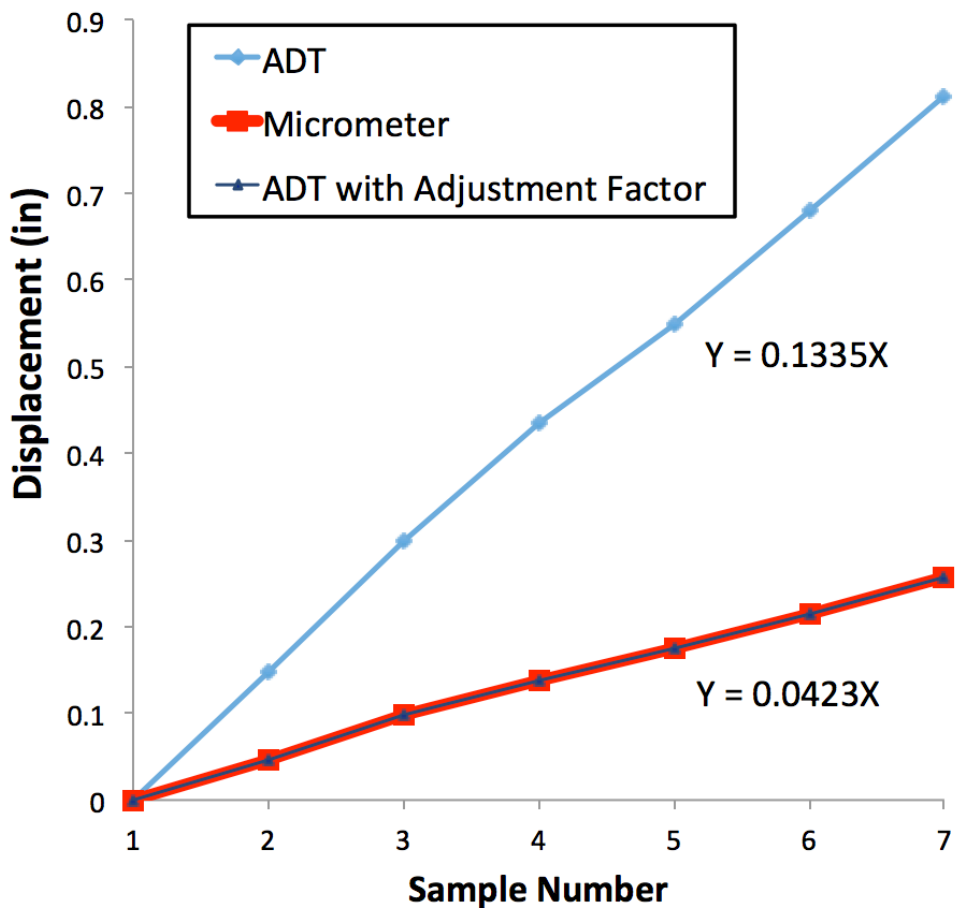


Figure 2.8: Plot of system displacement measurements taken with ADT, manually with a micrometer and the same ADT results plotted with an adjustment factor. Notice the adjusted ADT measurements match those taken with the micrometer.

A test was performed to determine if the connecting components of the system would creep under an applied load and affect the test results. A sample T-bone was fabricated from 718 Inconel and heat treated, which is the same material from which the specimen grips and connecting rods are fabricated. The sample was inserted into the specimen grips and the system put under a load of 35 MPa (the load used for subsequent sample testing). The system was tested for a 24 h duration. An initial displacement was recorded by the ADT within the first few seconds of the system coming under load,

which can be attributed to the elimination of slack in the system. No creep of the system components was detected for the duration of the 24 h period, demonstrating that the only contributing factor to subsequent tests' resulting creep was due to elongation of the T-bone specimens.

The furnace to heat the sample at a constant temperature was vertically aligned and therefore a temperature profile was conducted to ensure that the temperature felt by the test specimen was indeed the temperature set point being measured by the K-type thermocouple. A second thermocouple was inserted along the inside length of the furnace and used to identify the location at which the measured temperature matched that being displayed as the set point on the furnace power control cabinet. This test was repeated three times and the results averaged with a final location determined to be 5.5 inches measured from the top of the furnace tube or 6.5 inches measured from the tube bottom exit. The system cables were adjusted accordingly to ensure that when under load, the test specimen would be located at the target height.

For a constant-stress test, the equation:

$$P/P_0 = L_0/L \quad (1)$$

where  $P$  is the load and  $L$  is the length of the specimen, must be satisfied for any angle and for any initial load  $P_0$  in order to satisfy the requirement that  $PL = \text{constant}$ . The creep rig was calibrated by comparing the theoretical predictions of equation (1) with experimental measurements of  $P$  and  $L$ .

Before beginning the calibration test, the cam was adjusted so the horizontal position mark inscribed on its side was level and at the intended zero mark. The furnace door was propped open to expose the specimen grips inside and a test specimen inserted.

Steel balls with a total load 45 MPa were placed onto the loading tray. A zero reading was taken and recorded. The angle was increased in 5-degree increments, by mechanically simulating a displacement of the specimen, from 0 to 35 deg. For each interval, the load and linear displacement were recorded. Figure 2.9 shows the calibration plot. The experimental values had an average variation of 0.36 percent compared to the theoretically predicted values from equation (1). This value was well within the bounds of literature values <sup>41</sup> confirming the rig was calibrated and operational for constant-stress testing.

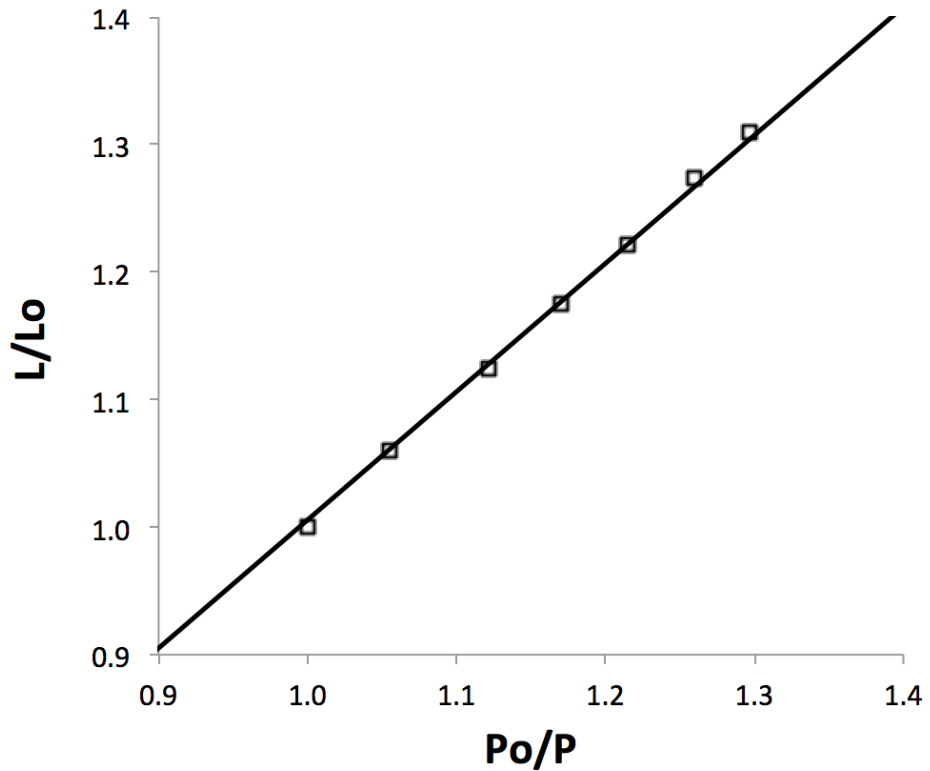


Figure 2.9: Load calibration of constant-stress cam

#### 2.3.4 Testing Procedure

With the completion of calibration testing, creep test specimens were milled from the Fe-20Cr-30Ni-2Nb-5Al model alloy as described in section 2.2.2 with the dimensions shown in Figure 2.10. Each specimen was homogenized for 24 h at 1250 °C as described in section 2.2.3 and subsequently heat-treated at 800 °C if required.

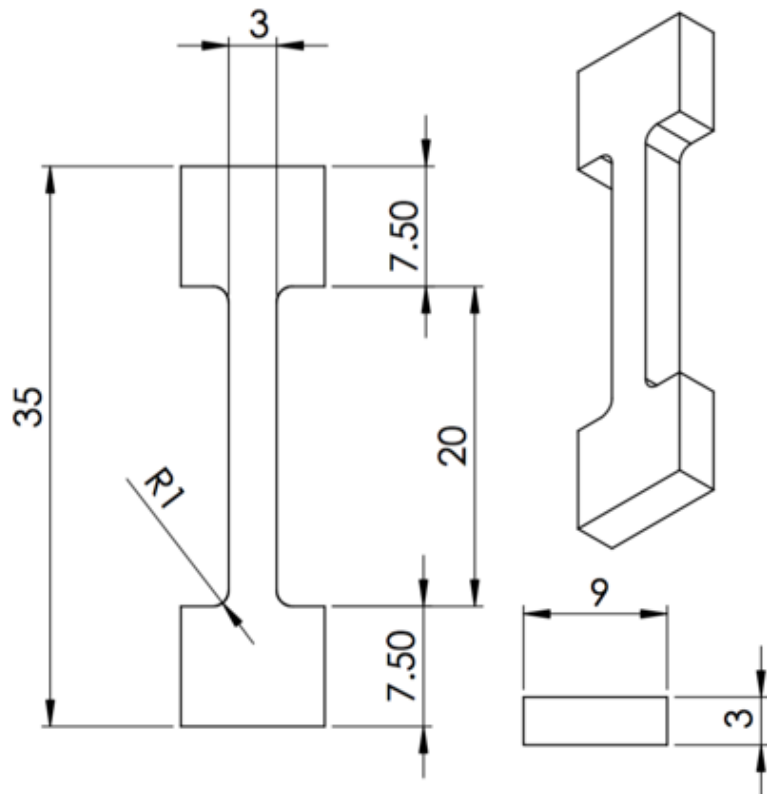


Figure 2.10: Dimensions of creep test specimen in millimeters.

Test specimens were inserted into the specimen grips and the furnace door locked. Glass wool was placed over the top and bottom furnace openings to reduce air currents and increase temperature uniformity. 8.852 lb were placed on the loading tray for a total load of 35 MPa, but not attached to the cam cable wire attachment loop. The cam was set so that the inscribed horizontal position mark was level and the furnace set to 760 °C. This temperature was chosen for all creep tests, because it matches the target application temperature for AFA stainless steels. Upon reaching the desired temperature,

the weighted loading tray was hooked on the wire cable attachment loop and the system put into tension. When the loading tray stabilized within a few seconds, the data record button on the data logger would be pressed to begin data logging. Temperature was held constant in each test.

At 760 °C and under a 35 MPa load, it was established that the model alloy tested would enter the secondary creep regime approximately one hour after the specimen was put into tension by loading. It would remain at a steady state for at least a 750 h duration (the longest duration tested). To capture a representative sample of the creep curve, the duration of each test was 500 h, with the exception of two shorter partial tests conducted to evaluate microstructural changes at stages on the creep curve.

Upon completion of a test, data recording would be terminated, the system unloaded and the furnace ramped down to room temperature. The test specimen would then be removed from the specimen grips and sectioned into three parts using a diamond saw as described in section 2.2.2. Figure 2.11 shows the locations of where each section was located on the T-bone. Each section was imaged using Scanning Electron Microscopy as detailed in the following section. These three locations were chosen to explore any differences in precipitate directionality visible during the microstructural analysis of each sample.

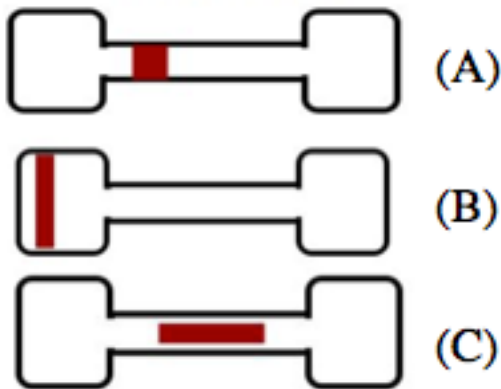


Figure 2.11: Post-creep T-bone cross-sections cut for SEM microstructural analysis. (A)

Square (B) Head (C) Middle-long

Creep curves of strain percent over time were produced from the load and displacement data collected. Details about the heat treatments and each test's duration can be found in the following chapter.

## 2.4 Materials Characterization

### 2.4.1 Scanning Electron Microscopy

In preparation for imaging with the Scanning Electron Microscope (SEM), samples were compression mounted and polished on a turntable using successively finer silicon carbide abrasive paper up to 1200-grit, then with 0.3  $\mu\text{m}$  followed by a finer 0.05  $\mu\text{m}$  alumina powder dissolved in water. Samples were placed on a polishing vibrometer with a thin layer of diluted MasterMet Colloidal Silica Polishing Suspension solution for  $\sim 3$  h to eliminate surface defects and achieve a mirror finish. After the polishing was complete, the samples were washed with a spray of distilled water, then methanol, followed by a light scrubbing with a cotton swab and detergent to eliminate any adhered alumina particles.

Samples were imaged using a Tescan Vega3 SEM outfitted with Bruker Quantax Energy-dispersive X-ray Spectroscopy (EDS) and electron backscatter diffraction (EBSD) detectors. Samples were imaged using back-scattered electrons (BSE) with a working distance of 10 mm and operating voltage of 15 keV.

#### *2.4.2 Mechanical Testing*

Flat T-bones approximately 1 mm thick, with a gauge length of 15 mm, and width of 2 mm were machined from the model alloy as detailed in section 2.2.2 and homogenized at 1250 °C for 24 h. Specimens were heat treated at 760 °C for 0, 2.4, 24 or 240 h and inserted into high-temperature specimen grips of the Instron 5690 tensile testing machine coupled with a MTS hydraulic testing machine. The metal frame of the Instron supports the Mellen Inc. SCR Split Series 120 V 1200 W Furnace mounted vertically. The furnace utilizes clamshell-heating elements capable of 1250 °C in air. The temperature was measured with a centrally located K-type thermocouple and controlled by a Mellen Inc. PS105 programmable power control cabinet.

Elevated temperature tensile tests were conducted at 760 °C with an applied preload force of 50 N. For all tests the initial strain rate was  $5 \times 10^{-4} \text{ s}^{-1}$ , and each tensile test was performed three times for each heat treatment protocol. True strain ( $\epsilon$ ) and true stress ( $\sigma$ ) were calculated from the load-displacement data and reported as true stress-strain curves. Percent elongation of the specimen was obtained by comparing the initial specimen gauge length and measuring the specimen gauge length after the tests were complete.

Elevated temperature strain-rate jump tests were conducted at 760 °C, with an applied preload force of 50N prior to testing. The initial strain for all tests was  $5 \times 10^{-5} \text{ s}^{-1}$

<sup>1</sup>. Each strain-rate jump was increased by an order of magnitude once a steady-state flow stress was obtained. The strain-rate jump test was performed three times for each specimen. True strain ( $\epsilon$ ) and true stress ( $\sigma$ ) were calculated from the load-displacement data and reported as true stress-strain curves.

## CHAPTER 3 EFFECT OF AGING TIME ON MICROSTRUCTURE AND HIGH TEMPERATURE CONSTANT-STRESS CREEP BEHAVIOR

### 3.1 Introduction

In this chapter, the effects of aging time on the microstructure and high temperature creep behavior of the model alloy Fe-20Cr-30Ni-2Nb-5Al (at.%) is investigated. Constant-stress creep tests were performed at an elevated temperature of 760 °C for specimens first homogenized at 1250 °C and then aged 0, 2.4, 24 or 240 h at 800 °C.

Microstructural analysis was performed on the specimens prior to and after each creep test. Microstructural evolution was studied for a non-aged homogenized sample at four points along the creep curve. The microstructural effects of straining at high temperature under a constant stress were also investigated, specifically by comparing precipitated particle quantity at two locations of a crept specimen: one in which the specimen did not feel strain and another at which it did.

### 3.2 Experimental

Creep test specimens were machined from Fe-20Cr-30Ni-2Nb-5Al (at. %) model alloy as described in section 2.2.2. T-bone test specimens were milled to a 3 mm thickness, with a gauge length of 20 mm, width of 3mm and overall length of 35 mm. Each specimen was homogenized for 24 h at 1250 °C as described in section 2.2.3 to produce a single phase material. Specimens were subsequently aged in air at 800 °C for 0, 2.4, 24 or 240 h.

Prior to undergoing creep tests, samples were imaged using a Tescan Vega3 SEM outfitted with Bruker Quantax Energy-dispersive X-ray Spectroscopy (EDS) and

electron backscatter diffraction (EBSD) detectors. Back-scattered electrons (BSE) with a working distance of 10 mm and operating voltage of 15 keV were used for microstructural analysis. In preparation for imaging, samples were compression mounted and polished on a turntable using successively finer silicon carbide abrasive paper up to 1200-grit, then with 0.3  $\mu\text{m}$  followed by a finer 0.05  $\mu\text{m}$  alumina powder dissolved in water. Samples were placed on a polishing vibrometer with a thin layer of diluted MasterMet Colloidal Silica Polishing Suspension solution for  $\sim$ 3 h. The samples were washed with a spray of distilled water, methanol and detergent as described in the materials characterization section on Experimental Methods.

Elevated temperature constant-stress creep tests were conducted for a duration of 500 h for each aging condition at 760  $^{\circ}\text{C}$  under a 35 MPa load. Each long term 500 h test conducted twice for each aging condition. Under the conditions tested, it was established that the model alloy would enter the secondary creep regime approximately one hour after the specimen was put into tension by loading. It would remain at a steady state for at least a 750 h duration (the longest duration tested). To capture a representative sample of the creep curve, the duration of each test was 500 h, with the exception of two shorter partial tests. Details of constant-stress creep test procedures may be found in the previous chapter's testing procedure section 2.3.4.

Two partial constant-stress creep tests were conducted to evaluate the alloy's microstructural changes as it crept over time. Similar test conditions as the full range 500 h creep tests were used for the partial tests. Two specimens were homogenized at 1250  $^{\circ}\text{C}$  but not aged. The first partial test (referred to from here on as "P1") was run for 3.5 h and

the second partial test (referred to from here on as “P2”) ran for a 300 h duration to get representative samples along the creep curve.

Upon completion of a test, the furnace was cooled to room temperature and the test specimen was removed from the specimen grips. Creep curves of strain percent over time were produced from the load and displacement data collected. The crept T-bone sample was sectioned into three parts using a diamond saw. Figure 3.1 shows the locations of each section on the T-bone. These three locations (Square, Head and Middle-long) were chosen to explore any differences in precipitate directionality or observable microstructural differences between the three sections. No visible difference was observable, but to quantify these findings, SEM images of a crept T-bone’s head and gauge section were compared side-by-side and the particle size quantified using ImageJ software.

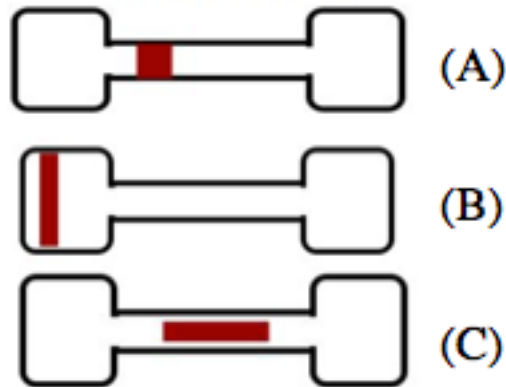


*Figure 3.1: Diagram detailing the locations of sections taken for SEM microstructural analysis from crept T-bones. (A) Square (B) Head (C) Middle-long*

Each crept sample was mounted, polished and imaged using the SEM.

### 3.3 Results and Discussion

#### 3.3.1 Effect of aging time on constant-stress creep rates and microstructure

### *3.2.2 Comparison of straining on crept specimens*

T-bone head to gauge comparison

### *3.2.3 Evolution of microstructure along constant-stress creep curve*

Particle Quantification

## CHAPTER 4 EFFECT OF AGING TIME ON HIGH TEMPERATURE TENSILE BEHAVIOR

### 4.1 Introduction

The current chapter investigates the effects of aging time on the model alloy Fe-20Cr-30Ni-2Nb-5Al (at.%) high temperature tensile behavior at 760 °C. Elevated temperature tensile tests and strain-rate jump tests were performed for specimens homogenized at 1250 °C and subsequently aged 0, 2.4, 24 or 240 h at 760 °C. The resulting true stress-strain curve results were studied and compared.

### 4.2 Experimental

#### 4.2.1 *Tensile tests at elevated temperature*

T-bone test specimens were milled from the Fe-20Cr-30Ni-2Nb-5Al model alloy as described in the materials preparation section 2.2.2 with the dimensions shown in Figure 4.1.

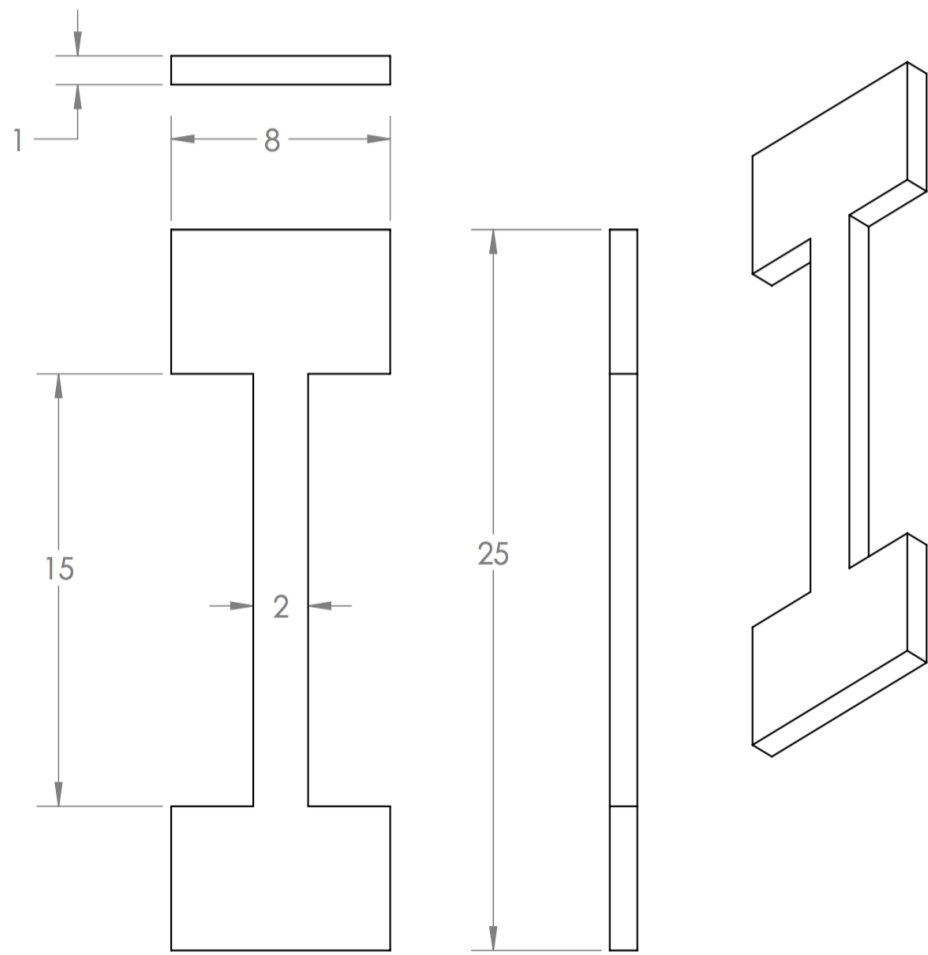


*Figure 4.1: Dimensions of tensile test specimen in millimeters.*

Each specimen was homogenized at 1250 °C for 24 h and aged at 760 °C for 0, 2.4, 24 or 240 h. Elevated temperature tensile tests were conducted at 760 °C with an applied preload force of 50 N. For all tests the initial strain rate was  $5 \times 10^{-4} \text{ s}^{-1}$ , and each tensile test was performed three times for each heat treatment protocol. True strain ( $\varepsilon$ ) and true stress ( $\sigma$ ) were calculated from the load-displacement data and reported as true stress-strain curves. Percent elongation of the specimen was obtained by comparing the initial specimen gauge length and measuring the specimen gauge length after the tests were complete.

#### *4.2.2 Strain-rate jump tests at elevated temperature*

T-bone test specimens were milled from the Fe-20Cr-30Ni-2Nb-5Al model alloy as described in the materials preparation section 2.2.2 with the dimensions shown in Figure 4.1. Each specimen was homogenized at 1250 °C for 24 h and aged at 760 °C for 0, 2.4, 24 or 240 h. Strain-rate jump tests were conducted at 760 °C, with an applied preload force of 50N prior to testing. The initial strain for all tests was  $5 \times 10^{-5} \text{ s}^{-1}$ . Each strain-rate jump was increased by an order of magnitude once a steady-state flow stress was obtained. The strain-rate jump test was performed three times for each specimen. True strain ( $\varepsilon$ ) and true stress ( $\sigma$ ) were calculated from the load-displacement data and reported as true stress-strain curves.

### **4.3 Results and Discussion**

#### *4.3.1 Tensile tests at elevated temperature*

#### *4.3.2 Strain-rate jump tests at elevated temperature*

## **CHAPTER 5 CONCLUSION**

Paragraph 1

Paragraph 2

Paragraph 3

## **CHAPTER 6 FUTURE WORK**

Future work should be divided into two main focus areas:

1. Abc

2. Abc

## 7 REFERENCES

1. Viswanathan, R., Armor, A. & BOORAS, G. A critical look at supercritical power plants. *Power* **148**, 42–49 (2004).
2. Viswanathan, R., Coleman, K. & Rao, U. Materials for ultra-supercritical coal-fired power plant boilers. *Int. J. Press. Vessels Pip.* **83**, 778–783 (2006).
3. Viswanathan, V., Purgert, R. & Rawls, P. Coal-fired power materials. *Adv Mater Process* **166**, 47–49 (2008).
4. Viswanathan, R. *et al.* US program on materials technology for ultra-supercritical coal power plants. *J. Mater. Eng. Perform.* **14**, 281–292 (2005).
5. Viswanathan, R. & Bakker, W. Materials for ultrasupercritical coal power plants—Boiler materials: Part 1. *J. Mater. Eng. Perform.* **10**, 81–95 (2001).
6. Yamamoto, Y. *et al.* Creep-resistant, Al<sub>2</sub>O<sub>3</sub>-forming austenitic stainless steels. *Science* **316**, 433–436 (2007).
7. Viswanathan, R. & Bakker, W. Materials for boilers in ultra supercritical power plants. in *Proceedings of 2000 International Joint Power Generation Conference* **20**, (Miami Beach, Florida, 2000).
8. Yamamoto, Y. *et al.* Alumina-Forming Austenitic Stainless Steels Strengthened by Laves Phase and MC Carbide Precipitates. *Metall. Mater. Trans. A* **38**, 2737–2746 (2007).
9. Brady, M. P., Yamamoto, Y., Santella, M. L. & Pint, B. A. Effects of minor alloy additions and oxidation temperature on protective alumina scale formation in creep-resistant austenitic stainless steels. *Scr. Mater.* **57**, 1117–1120 (2007).
10. Brady, M. P. *et al.* The development of alumina-forming austenitic stainless steels for high-temperature structural use. *JOM* **60**, 12–18 (2008).

11. Pint, B. A., Shingledecker, J. P., Brady, M. P. & Maziasz, P. J. Alumina-forming austenitic alloys for advanced recuperators. *ASME Pap. No GT2007-27916* (2007).
12. Brady, M. P., Yamamoto, Y., Santella, M. L. & Walker, L. R. Composition, microstructure, and water vapor effects on internal/external oxidation of alumina-forming austenitic stainless steels. *Oxid. Met.* **72**, 311–333 (2009).
13. Yamamoto, Y., Santella, M. L., Brady, M. P., Bei, H. & Maziasz, P. J. Effect of Alloying Additions on Phase Equilibria and Creep Resistance of Alumina-Forming Austenitic Stainless Steels. *Metall. Mater. Trans. A* **40**, 1868–1880 (2009).
14. Brady, M. P., Magee, J., Yamamoto, Y., Helmick, D. & Wang, L. Co-optimization of wrought alumina-forming austenitic stainless steel composition ranges for high-temperature creep and oxidation/corrosion resistance. *Mater. Sci. Eng. A* **590**, 101–115 (2014).
15. Yamamoto, Y., Muralidharan, G. & Brady, M. P. Development of L1 2-ordered Ni 3 (Al, Ti)-strengthened alumina-forming austenitic stainless steel alloys. *Scr. Mater.* **69**, 816–819 (2013).
16. Yamamoto, Y. *et al.* Alloying effects on creep and oxidation resistance of austenitic stainless steel alloys employing intermetallic precipitates. *Intermetallics* **16**, 453–462 (2008).
17. Yamamoto, Y. *et al.* Overview of strategies for high-temperature creep and oxidation resistance of alumina-forming austenitic stainless steels. *Metall. Mater. Trans. A* **42**, 922–931 (2011).
18. Kofstad, P. & Bredesen, R. High temperature corrosion in SOFC environments. *Solid State Ion.* **52**, 69–75 (1992).

19. Pint, B. A., Distefano, J. R. & Wright, I. G. Oxidation resistance: One barrier to moving beyond Ni-base superalloys. *Mater. Sci. Eng. A* **415**, 255–263 (2006).
20. Pint, B. A., Peraldi, R. & Maziasz, P. J. The use of model alloys to develop corrosion-resistant stainless steels. in *Materials Science Forum* **461**, 815–822 (Trans Tech Publ, 2004).
21. Brady, M. P. *et al.* *Oxidation resistant high creep strength austenitic stainless steel*. (Google Patents, 2010).
22. Yamamoto, Y., Brady, M. P., Lu, Z. P. & Liu, C. Multi-phase high temperature alloys: exploration of laves-strengthened steels. in *Annual Conference On Fossil Energy Materials* 20–27 (Citeseer, 2006).
23. Cahn, J. W. Nucleation on dislocations. *Acta Metall.* **5**, 169–172 (1957).
24. Porter, D. A., Easterling, K. E. & Sherif, M. *Phase Transformations in Metals and Alloys, (Revised Reprint)*. (CRC press, 2009).
25. Chen, S., Zhang, C., Xia, Z., Ishikawa, H. & Yang, Z. Precipitation behavior of Fe 2 Nb Laves phase on grain boundaries in austenitic heat resistant steels. *Mater. Sci. Eng. A* **616**, 183–188 (2014).
26. Pint, B. A. *et al.* Development of alumina-forming austenitic alloys for advanced recuperators. in *ASME Turbo Expo 2009: Power for Land, Sea, and Air* 271–280 (American Society of Mechanical Engineers, 2009).
27. Sourmail, T. Precipitation in creep resistant austenitic stainless steels. *Mater. Sci. Technol.* **17**, 1–14 (2001).
28. Abe, F., Taneike, M. & Sawada, K. Alloy design of creep resistant 9Cr steel using a dispersion of nano-sized carbonitrides. *Int. J. Press. Vessels Pip.* **84**, 3–12 (2007).

29. Stott, F., Wood, G. & Stringer, J. The influence of alloying elements on the development and maintenance of protective scales. *Oxid. Met.* **44**, 113–145 (1995).
30. Kato, Y., Ito, M., Kato, Y. & Furukimi, O. Effect of Si on Precipitation Behavior of Nb-Laves Phase and Amount of Nb in Solid Solution at Elevated Temperature in High Purity 17% Cr-0.5% Nb Steels. *Mater. Trans.* **51**, 1531–1535 (2010).
31. Liu, C., Zhu, J., Brady, M., McKamey, C. & Pike, L. Physical metallurgy and mechanical properties of transition-metal Laves phase alloys. *Intermetallics* **8**, 1119–1129 (2000).
32. Trotter, G. & Baker, I. The effect of aging on the microstructure and mechanical behavior of the alumina-forming austenitic stainless steel Fe–20Cr–30Ni–2Nb–5Al. *Mater. Sci. Eng. A* **627**, 270–276 (2015).
33. Cao, W. & Kennedy, R. Superalloys 718, 625, 706 and Various Derivatives, ed. EA Loria *TMS* 455–464 (2001).
34. Massalski, T. B., Murray, J. L., Bennett, L. H. & Baker, H. Binary Alloy Phase Diagrams; American Society for Metals: Metals Park, OH, 1986. *There No Corresp. Rec. This Ref.* (1904).
35. Villars, P., Prince, A. & Okamoto, H. *Handbook of ternary alloy phase diagrams*. (Asm Intl, 1995).
36. Tarigan, I., Kurata, K., Takata, N., Matsuo, T. & Takeyama, M. Novel Concept of Creep Strengthening Mechanism using Grain Boundary Fe 2 Nb Laves Phase in Austenitic Heat Resistant Steel. in *MRS Proceedings* **1295**, mrsf10–1295 (Cambridge Univ Press, 2011).
37. Tarigan, I., Takata, N. & Takeyama, M. Grain boundary precipitation strengthening mechanism by Fe2Nb Laves phase in creep of Fe-20Cr-30Ni-2Nb austenitic heat resistant

- steel. in *Proceedings of the 12th International Conference on Creep and Fracture of Engineering Materials and Structure (JIMIS 11)* (2012).
38. Brady, M. P. *et al.* On the loss of protective scale formation in creep-resistant, alumina-forming austenitic stainless steels at 900 C in air. in *Materials Science Forum* **595**, 725–732 (Trans Tech Publ, 2008).
  39. Satyanarayana, D., Malakondaiah, G. & Sarma, D. Characterization of the age-hardening behavior of a precipitation-hardenable austenitic steel. *Mater. Charact.* **47**, 61–65 (2001).
  40. Satyanarayana, D., Malakondaiah, G. & Sarma, D. Steady state creep behaviour of NiAl hardened austenitic steel. *Mater. Sci. Eng. A* **323**, 119–128 (2002).
  41. Garofalo, F., Richmond, O. & Domis, W. F. Design of apparatus for constant-stress or constant-load creep tests. *J. Basic Eng.* **84**, 287–293 (1962).
  42. da C. Andrade, E. N. & Chalmers, B. The Resistivity of Polycrystalline Wires in Relation to Plastic Deformation, and the Mechanism of Plastic Flow. *Proc. R. Soc. Lond. Math. Phys. Eng. Sci.* **138**, 348–374 (1932).

## APPENDICES

### Appendix I

#### CONSTANT STRESS DERIVATION

To maintain a constant stress, the following condition must be satisfied:

$$rL = \text{constant} = r_0 L_0 \quad (1)$$

Where:

$L_0$  = initial specimen length

$r_0$  = initial value of  $r$  (instantaneous moment arm of the applied weight)

The instantaneous specimen length can be written as:

$$L = L_0 + (\theta - \theta_0)R \quad (2)$$

Where:

$\theta_0$  = angle for initial positioning of constant-stress cam

Eliminating  $L$  from equations (1) and (2) gives you the equation for the profile of a constant-stress cam:

$$r = \frac{r_0 L_0}{L_0 + R(\theta - \theta_0)} \quad (3)$$

This equation needs to be transformed into fixed a Cartesian coordinate system for ease of use in terms of  $x$  and  $y$ .

$$x = r \cos(\theta) + z \sin(\theta) \quad (4)$$

$$y = r \sin(\theta) - z \cos(\theta) \quad (5)$$

$$\frac{dx}{dy} = -\tan(\theta) \quad (6)$$

Eliminating  $x$  and  $y$  from the equations:

$$z = -dr/d\theta = \frac{r_0 L_0 R}{[L_0 + R(\theta - \theta_0)]^2} \quad (7)$$

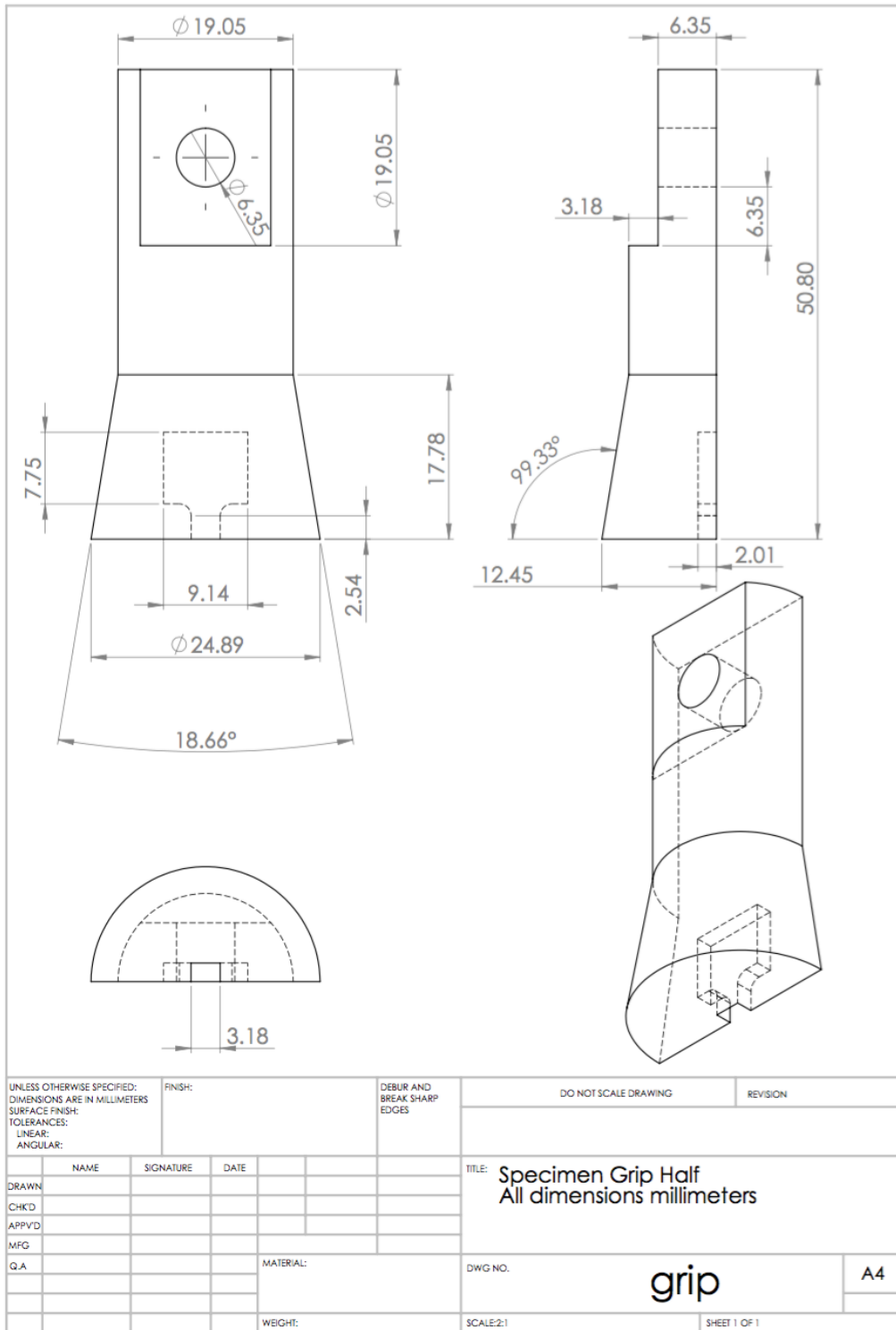
Substituting the above equation and equation (3) into equations (4) and (5) yields the fixed coordinates of the constant-stress cam in terms of the single parameter  $\theta$ :

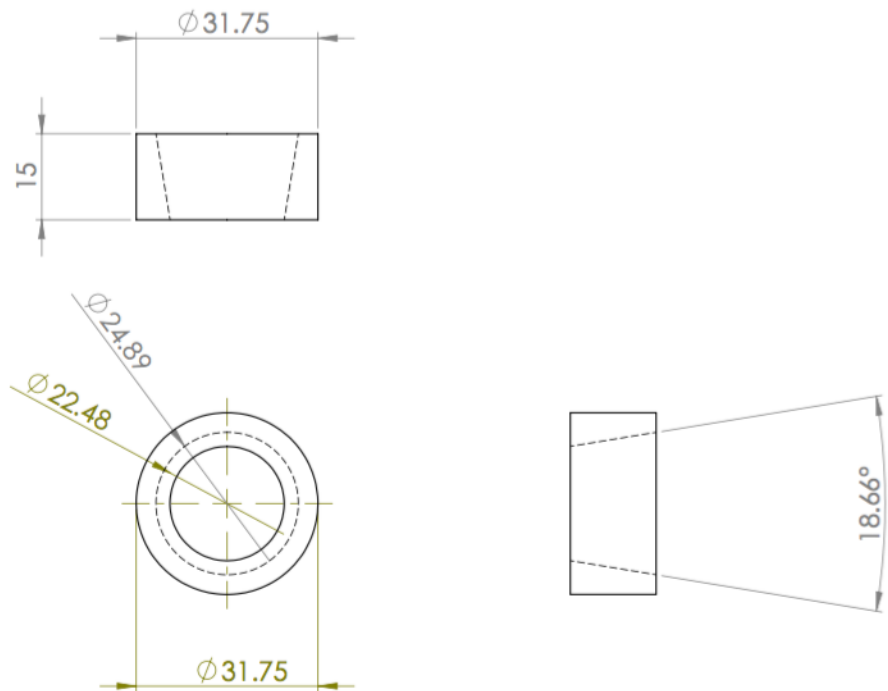
$$x = \frac{a}{1 + b\theta} \left[ \cos(\theta) + \frac{b \sin(\theta)}{1 + b\theta} \right] \quad (8)$$

$$y = \frac{a}{1 + b\theta} \left[ \sin(\theta) - \frac{b \cos(\theta)}{1 + b\theta} \right] \quad (9)$$

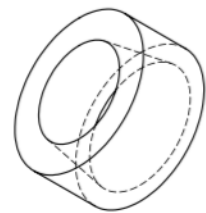
Where:  $a = \frac{r_0 L_0}{L_0 - R\theta_0}$  and  $b = \frac{R}{L_0 - R\theta_0}$

## Appendix II

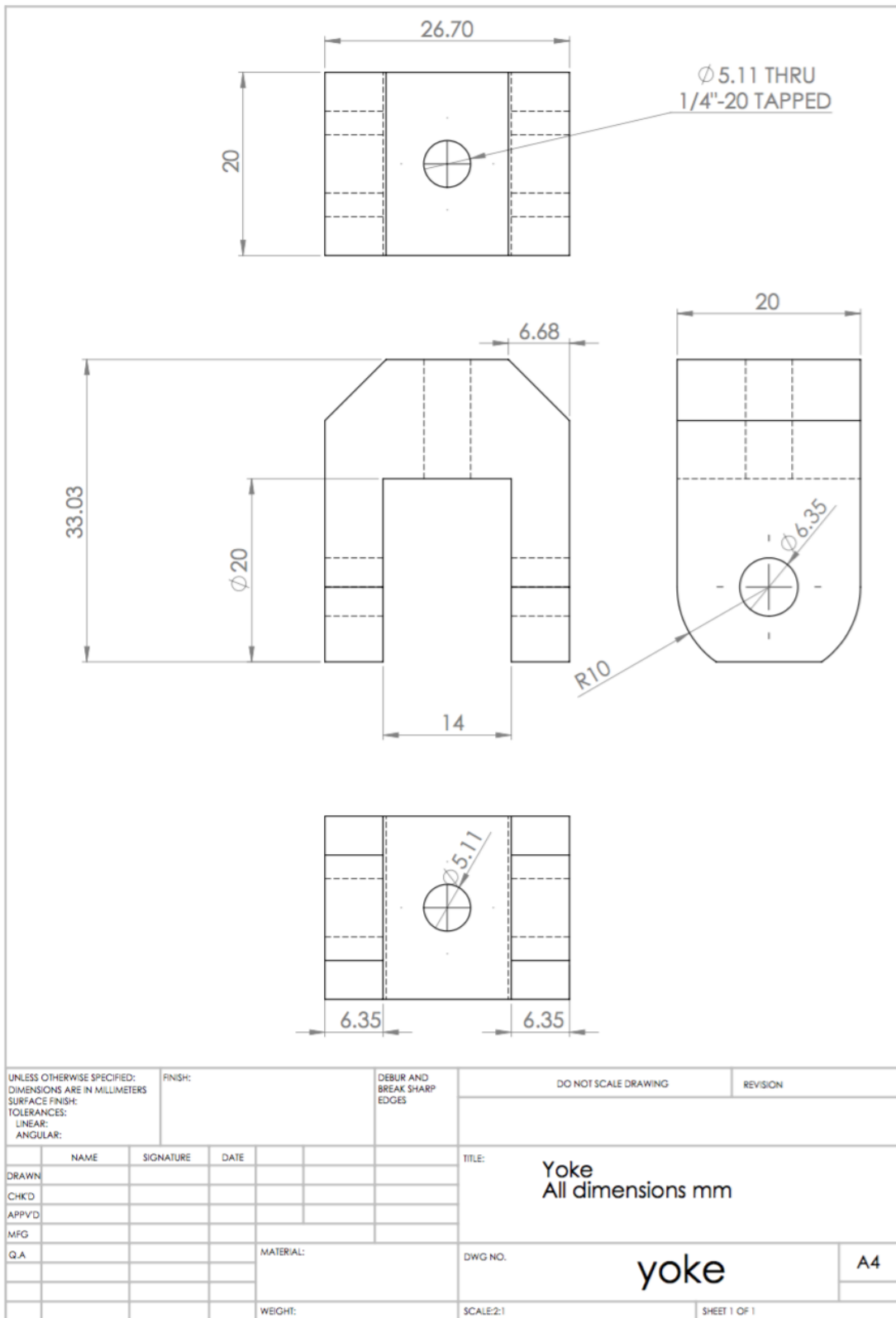


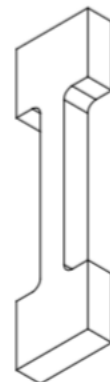
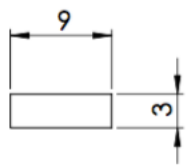
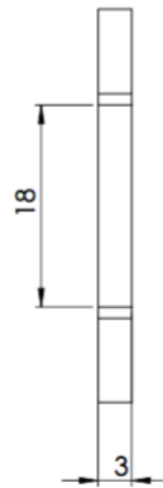
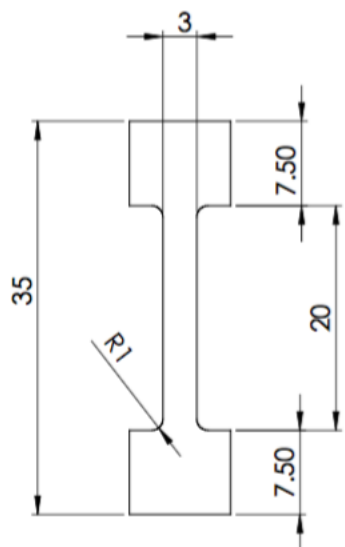


Grip Collet  
All dimensions millimeters



UNLESS OTHERWISE SPECIFIED: DIMENSIONS ARE IN MILLIMETERS SURFACE FINISH: TOLERANCES: LINEAR: ANGULAR:			FINISH:		DEBUR AND BREAK SHARP EDGES	DO NOT SCALE DRAWING		REVISION
DRAWN	NAME	SIGNATURE	DATE			TITLE:		
CHKD								
APPVD								
MFG								
QA					MATERIAL:	DWG NO.	collet	
								A4
				WEIGHT:		SCALE:1:1	SHEET 1 OF 1	





Tensile Specimen  
All dimensions millimeters

UNLESS OTHERWISE SPECIFIED: DIMENSIONS ARE IN MILLIMETERS SURFACE FINISH: TOLERANCES: LINEAR: ANGULAR:		FINISH:		DEBUR AND BREAK SHARP EDGES	DO NOT SCALE DRAWING	REVISION
DRAWN	NAME	SIGNATURE	DATE			
CHKD						
APP'D						
MFG						
QA				MATERIAL:	DWG NO.	A4
			WEIGHT:		specimen	
				SCALE:2:1	SHEET 1 OF 1	

